



Metal-enriched Neutral Gas Reservoir around a Strongly Lensed Low-mass Galaxy at $z = 4$ Identified by JWST/NIRISS and VLT/MUSE

Downloaded from: <https://research.chalmers.se>, 2025-12-04 09:37 UTC

Citation for the original published paper (version of record):

Lin, X., Cai, Z., Zou, S. et al (2023). Metal-enriched Neutral Gas Reservoir around a Strongly Lensed Low-mass Galaxy at $z = 4$ Identified by JWST/NIRISS and VLT/MUSE. *Astrophysical Journal Letters*, 944(2).
<http://dx.doi.org/10.3847/2041-8213/aca1c4>

N.B. When citing this work, cite the original published paper.



Metal-enriched Neutral Gas Reservoir around a Strongly Lensed Low-mass Galaxy at $z=4$ Identified by JWST/NIRISS and VLT/MUSE

Xiaojing Lin¹, Zheng Cai¹, Siwei Zou¹, Zihao Li¹, Zuyi Chen², Fuyan Bian³, Fengwu Sun², Yiping Shu⁴, Yunjing Wu^{1,2}, Mingyu Li¹, Jianan Li¹, Xiaohui Fan², J. Xavier Prochaska^{5,6}, Daniel Schaerer⁷, Stephane Charlot⁸, Daniel Espada^{9,10}, Miroslava Dessauges-Zavadsky¹¹, Eiichi Egami², Daniel Stark², Kirsten K. Knudsen¹², Gustavo Bruzual¹³, and Jacopo Chevallard¹⁴

¹ Department of Astronomy, Tsinghua University, Beijing 100084, People's Republic of China; zcaai@mail.tsinghua.edu.cn

² Steward Observatory, University of Arizona, 933 N Cherry Avenue, Tucson, AZ 85721, USA

³ European Southern Observatory, Alonso de Córdova 3107, Casilla 19001, Vitacura, Santiago 19, Chile

⁴ Purple Mountain Observatory, Chinese Academy of Sciences, 10 Yuan Hua Road, Nanjing, Jiangsu 210023, People's Republic of China

⁵ Department of Astronomy and Astrophysics, UCO, Lick Observatory, University of California 1156 High Street, Santa Cruz, CA 95064, USA

⁶ Kavli IPMU, the University of Tokyo (WPI), Kashiwa 277-8583, Japan

⁷ Observatoire de Genève, Université de Genève, Chemin Pegasi 51, CH-1290 Versoix, Switzerland

⁸ Sorbonne Université, CNRS, UMR7095, Institut d'Astrophysique de Paris, F-75014, Paris, France

⁹ Departamento de Física Teórica y del Cosmos, Campus de Fuentenueva, Edificio Mecenas, Facultad de Ciencias, Universidad de Granada, E-18071, Granada, Spain

¹⁰ Instituto Carlos I de Física Teórica y Computacional, Facultad de Ciencias, E-18071, Granada, Spain

¹¹ Department of Astronomy, University of Geneva, Chemin Pegasi 51, 1290 Versoix, Switzerland

¹² Institutionen för rymd-, geo- och miljövetenskap, Department of Space, Earth and Environment Chalmers tekniska högskola, Chalmers University of Technology, Sweden

¹³ Institute of Radio Astronomy and Astrophysics, National Autonomous University of Mexico, San José de la Huerta 58089 Morelia, Michoacán, México

¹⁴ Department of Physics, University of Oxford, Denys Wilkinson Building, Keble Road, Oxford OX1 3RH, UK

Received 2022 September 7; revised 2022 October 30; accepted 2022 November 10; published 2023 March 2

Abstract

Direct observations of low-mass, low-metallicity galaxies at $z \gtrsim 4$ provide an indispensable opportunity for detailed inspection of the ionization radiation, gas flow, and metal enrichment in sources similar to those that reionized the universe. Combining the James Webb Space Telescope (JWST), Very Large Telescope/MUSE, and Atacama Large Millimeter/submillimeter Array, we present detailed observations of a strongly lensed, low-mass ($\approx 10^{7.6} M_\odot$) galaxy at $z = 3.98$ (also see Vanzella et al.). We identify strong narrow nebular emission, including C IV $\lambda\lambda 1548, 1550$, He II $\lambda 1640$, O III $\lambda\lambda 1661, 1666$, [Ne III] $\lambda 3868$, [O II] $\lambda 3727$, and the Balmer series of hydrogen from this galaxy, indicating a metal-poor H II region ($\lesssim 0.12 Z_\odot$) powered by massive stars. Further, we detect a metal-enriched damped Ly α system (DLA) associated with the galaxy with the H I column density of $N_{\text{HI}} \approx 10^{21.8} \text{ cm}^{-2}$. The metallicity of the associated DLA may reach the supersolar metallicity ($\gtrsim Z_\odot$). Moreover, thanks to JWST and gravitational lensing, we present the resolved UV slope (β) map at the spatial resolution of $\approx 100 \text{ pc}$ at $z = 4$, with steep UV slopes reaching $\beta \approx -2.5$ around three star-forming clumps. Combining with low-redshift analogs, our observations suggest that low-mass, low-metallicity galaxies, which dominate reionization, could be surrounded by a high covering fraction of the metal-enriched, neutral-gaseous clouds. This implies that the metal enrichment of low-mass galaxies is highly efficient, and further supports that in low-mass galaxies, only a small fraction of ionizing radiation can escape through the interstellar or circumgalactic channels with low-column-density neutral gas.

Unified Astronomy Thesaurus concepts: Circumgalactic medium (1879); Interstellar absorption (831); Interstellar medium (847); Metallicity (1031); Metal line absorbers (1032); Stellar populations (1622)

1. Introduction

It is now believed that low-mass galaxies significantly contribute the major fraction of the ionization photons in the epoch of reionization (e.g., Atek et al. 2015; Bouwens et al. 2016). Observations of faint galaxies at high redshift, though very difficult, are required, especially in the era of the James Webb Space Telescope (JWST), to directly constrain the ionization radiation, gas environment, galaxy growth, and metal enrichment of the surrounding intergalactic medium (IGM).

Extensive efforts have been conducted to study the intrinsic ultraviolet (UV) continuum and the ionization of low-mass galaxies. The UV continuum slope β ($f_\lambda \propto \lambda^\beta$) reveals crucial

properties of high-redshift galaxies. It is believed that young stellar population and intense star formation in early galaxies lead to very blue UV slopes (e.g., Schaerer 2003), even reaching -3 with extremely efficient ionizing agents with minimal dust reddening (e.g., Topping et al. 2022). The high spatial resolution of JWST enables studies on spatial variations of β , mapping the distribution of stellar populations and star-forming regions within early galaxies, often with clumpy structures, on subkiloparsec scales (Chen et al. 2022).

A great many studies aim to understand how ionization radiation escapes into the IGM (e.g., Ramambason et al. 2020). Before UV photons reach the IGM, how much radiation can escape from galaxies depends on (1) the intrinsic intensity and the slope of UV spectra and (2) the distribution of optically thick neutral hydrogen (H I) gas in the interstellar and circumgalactic medium (CGM; e.g., Chisholm et al. 2018). It is therefore crucial to study both UV continua and gas properties around low-mass galaxies to quantify the H I



Original content from this work may be used under the terms of the [Creative Commons Attribution 4.0 licence](https://creativecommons.org/licenses/by/4.0/). Any further distribution of this work must maintain attribution to the author(s) and the title of the work, journal citation and DOI.

(Ly α) optical depth in the CGM for better understanding the reionization process.

The existence of the neutral gas in and around low-mass star-forming galaxies has been suggested mainly through observations of Ly α emission (e.g., Gronke et al. 2017; Stark et al. 2017). Low-mass galaxies often have strong Ly α and other ionized nebular emission (e.g., Erb et al. 2010; Stark et al. 2014). The presence of optically thick, H I “shell” makes the Ly α emission showing the double-peak structure (e.g., Yang et al. 2017), with the expanding outflow further suppressing blue peaks of Ly α emission (Yang et al. 2014).

Nevertheless, only through emission, the nature of the interplay between the neutral gas and galaxy cannot be completely understood. Detailed gas properties, including the gas metallicity, geometry and density need to be constrained. The strong lensing, plus the deep integration of JWST and the Very Large Telescope (VLT)/MUSE, provides us with an excellent opportunity to conduct direct and detailed observations of a low-mass galaxy at $z=4$, through both emission and absorption. Here, we present a detailed analysis of a strongly magnified arclet galaxy in the Abell2744 field, combined with optical, infrared, and millimeter observations. The system is lensed into three multiple images, and the arclet is composed of two of them lying on both sides of the critical line, with three bright compact clumps (knots in the arc) mirrored on each side (Mahler et al. 2018; Bergamini et al. 2022). We name this galaxy “A2744-arc3.” It was also reported in Vanzella et al. (2022). Through spectral-energy-distribution (SED) fitting, they found that these clumps are gravitationally bound young massive star clusters with bursty star formation.

In this paper, we probe detailed properties of the interstellar and CGM of A2744-arc3. With VLT/MUSE and JWST, we provide detailed analysis of both nebular emission and absorption lines. Copious emission lines, including the detection of C IV $\lambda\lambda 1548, 1550$, He II $\lambda 1640$, O III] $\lambda\lambda 1661, 1666$, [Ne III] $\lambda 3868$, [O II] $\lambda 3727$, and Balmer series of hydrogen, allow us to quantify the low metallicity of the ionized medium (e.g., Smit et al. 2017; Witstok et al. 2021). Further, the high signal-to-noise (S/N) observations of absorption enable us, for the first time, to examine the detailed properties of the neutral gas reservoir surrounding a low-mass galaxy at $z \approx 4$. The excellent delensed spatial resolution down to ≈ 100 pc in rest-frame UV observations allow the examination of the spatial variations of the UV radiation. All these information yield unparalleled understanding of low-mass, young galaxies at high redshift using A2744-arc3 as a textbook example.

This paper is organized as follows. In Section 2, we describe the observations and data reduction, including JWST/NIRISS imaging and spectroscopy, Hubble Space Telescope (HST) imaging, VLT/MUSE and ALMA continuum observations. In Section 3, we provide details of photometry, SED fitting, and the lensing reconstruction in source plane. We also show the spatially resolved UV slope map. In Section 4, we present further analysis on the rest-frame UV and optical spectrum of A2744-arc3, including the analysis of both emission and absorption features. Discussions are conducted in Section 5. We assume a flat cosmological model with $\Omega_M = 0.3$, $\Omega_\Lambda = 0.7$, and $H_0 = 70 \text{ km s}^{-1} \text{ Mpc}^{-1}$. The GlaGic lensing model (Oguri 2010; Kawamata et al. 2016) is adopted.

2. Data

2.1. JWST/NIRISS Imaging and Grism Observations

NIRISS observations of A2744 were taken by the GLASS JWST Early Release Science Program (Treu et al. 2022), devoting about $2834.504 \text{ s} \approx 0.79 \text{ hr}$ for F115W, F150W, and F200W direct imaging, respectively. Especially the NIRISS/F200W data, spanning from 1.7 to $2.2 \mu\text{m}$, allows us to better improve constraints on its stellar mass. The data were reduced in the same way as shown in Wu et al. (2022). Here we summarize the procedure as follows: the data were reduced using the standard JWST pipeline¹⁵ v1.6.2 with calibration reference files “jwst_0944.pmap;” 1/f noise (see Schlawin et al. 2020) was modeled and removed using the code `tshirt/roeba`,¹⁶ and the “snowball” artifacts from cosmic rays (Rigby et al. 2022) were identified and masked; the world coordinate system of mosaicked images were registered using the Pan-STARRS1 catalog (Flewelling et al. 2020); the pixel scale of final mosaicked images was resampled to $0''.03$ with `pixfrac` = 0.8. We reduced NIRISS grism data using GRIZLI,¹⁷ and the 2D grism spectra were drizzled with a pixel scale $0''.065$.

To optimally extract 1D spectra of A2744-arc3, we first split the entire arclet into six segments, each with one clump. We extracted their 1D spectra using fifth Chebyshev polynomials. We summed over five 1D spectra of the six segments to get the final spectra. One of them was excluded since it is severely contaminated by zeroth- and first-order images from other sources.

2.2. Hubble Frontier Fields Images

The A2744 cluster was observed as part of the Hubble Space Telescope Frontier Fields program¹⁸ (ID: 13495, PI: J. Lotz) between 2013 October 25 and 2014 July 1 for 164.5 orbits in total, in three filters with the Advanced Camera for Surveys (ACS; F435W, F606W, and F814W) and four with the Wide Field Camera 3 (WFC3; F105W, F125W, F140W, and F160W). The high-level science product released by Space Telescope Science Institute with a pixel size of 30 mas is used in this study.

2.3. VLT/MUSE Observation

Multi Unit Spectroscopic Explorer (MUSE) observations toward A2744 were taken by the GTO Program 094.A-0115 (PI: Richard) between 2014 September and 2015 October, with a $2' \times 2'$ designed mosaic of pointings centered at $\alpha = 00^{\text{h}}14^{\text{m}}20^{\text{s}}.952$ and $\delta = -30^{\circ}23'53''.88$ (Mahler et al. 2018). Each pointing was observed for a total of 3.5, 4, 4, and 5 hr in addition to 2 hr at the cluster center. The publicly available data cube¹⁹ is adopted in this work.

2.4. ALMA Continuum Observations

The millimeter continuum observations are obtained from the ALMA Lensing Cluster Survey. A2744 is observed by ALMA band 6 (Program 2018.1.00035.L, PI: Kohnno;

¹⁵ <https://github.com/spacetelescope/jwst>

¹⁶ <https://github.com/eas342/tshirt>

¹⁷ <https://github.com/gbrammer/grizli/>

¹⁸ <https://archive.stsci.edu/prepds/frontier/>

¹⁹ <http://muse-vlt.eu/science/a2744/>

2013.1.00999.S, PI: Bauer), which covers a frequency range with two tunings of 250.0–257.5 GHz and 265.0–272.5 GHz, corresponding to wavelengths of ~ 1.15 mm (Sun et al. 2022). The 1σ continuum sensitivity or say rms is $45 \mu\text{Jy beam}^{-1}$. The data were reduced using the standard pipeline with the CASA (McMullin et al. 2007) with natural weighting, and will be described in details in S. Fujimoto et al. (2022, in preparation). This leads to a synthesized beam size (FWHM) of $\sim 1''$, corresponding to ~ 6.9 kpc at $z \sim 4$.

3. Result and Analysis

3.1. Photometry and SED Fitting

We use a box aperture along A2744-arc3 to carry out the photometry on seven broadband HST observations (ACS/F435W, F606W, F814W and WFC3/F105W, F125W, F140W, and F160W) and three JWST NIRISS observations (NIRISS/F115W, F150W, and F200W). For each band, the length and width of the box aperture are designed to match the 2σ contours of the arc, where σ is determined by the local sky background. A Sérsic modeling is performed to the nearest source in the north to exclude potential light contamination. Magnification and multi-image effects are corrected to determine the delensed flux. The median magnification along the arc is about 45 according to the Glafic model. We repeat the photometry and SED analysis using Richard et al. (2021) model, as described in Appendix A, and yield consistent results.

We perform SED modeling with the Bayesian code BEAGLE (Chevallard & Charlot 2016). We assume a constant star formation history, the dust extinction curve of the Small Magellanic Cloud with the optical depth in the V band varying in the range 0–0.5, and the Chabrier (2003) initial mass function with an upper limit of $300M_{\odot}$. The metallicity of the interstellar medium is kept the same as that of the stellar populations. A flat prior is applied for metallicity, $0.01 < Z/Z_{\odot} < 0.2$, and ionization parameter (the dimensionless ratio of the number density of H-ionizing photons to that of hydrogen) in log space, $-3 < \log U < -1$, for nebular emission (Gutkin et al. 2016). These priors are chosen on the basis of detections of the UV emission lines (see Section 4.2 for more details). A JWST NIRISS/F150W view of A2744-arc3, the SED fitting results, and the NIRISS grism 2D and 1D spectra are shown in Figure 1. It implies that A2744-arc3 is a young, low-mass galaxy with massive star formation, accompanied by blue UV slopes, strong nebular emission lines and a faint intrinsic UV luminosity. The absence of a Balmer break in the NIRISS spectrum further confirms a young stellar age. The continuum of ALMA band 6 at rest-frame 0.23 mm shows no clear detection, which indicates a 3σ upper limit of far-infrared luminosity surface density $< 2.2 \times 10^{11} L_{\odot} \text{ arcsec}^{-2}$ assuming a dust temperature $T = 35$ K and dust emissivity spectral index $b = 1.6$. This corresponds to an upper limit of star formation rate (SFR) surface density $\approx 9 \times 10^{-7} M_{\odot} \text{ yr}^{-1} \text{ pc}^{-2}$ (Murphy et al. 2011) and an upper limit of dust mass surface density $\approx 1.6 M_{\odot} \text{ pc}^{-2}$ (da Cunha et al. 2013).

In Vanzella et al. (2022), SED analysis was performed on each mirrored clump using images from NIRISS/F115W, F150W, F200W, and HST/WFC3 F105W, F125W, F140W, F160W, along with the ground-based VLT/HAWKI Ks band. Their derived SFR is $1.47^{+0.85}_{-0.25} M_{\odot} \text{ yr}^{-1}$, total stellar mass of $1.6^{+0.4}_{-1.3} \times 10^8 M_{\odot}$ (Table 1, 3c), and age of 126^{+33}_{-108} Myr. Our derived properties are marginally consistent with theirs within 1σ . They found that these nucleated star-forming regions have optical/

UV effective radii spanning 3–20 pc, bursty star formation activities ($\sim 10 \text{ Gyr}^{-1}$), and UV slopes of $\beta \simeq -1.9$, and stellar mass surface densities resembling those of local globular clusters. Our conclusion is consistent with theirs. Note that the upper limit of infrared-based SFR density is smaller than that obtained from UV ($\gtrsim 10^{-5} M_{\odot} \text{ yr}^{-1} \text{ pc}^{-2}$ for clumps in Vanzella et al. 2022), and this may be due to a low dust-obscured fraction of SFR in this low-mass galaxy with negligible dust content.

3.2. Source-plane Reconstruction and Spatially Resolved UV Slope

To explore the spatially resolved UV slope variation, we construct UV slope β maps in both the image plane and source plane using HST and JWST broadband images. We recover the intrinsic source morphology by ray tracing back the image-plane pixels on a regular source-plane grid based on the corresponding deflection field (Patrício et al. 2016). More details about the selection of lensing models and the reconstruction are presented in Appendix A.

The image-plane and reconstructed source-plane UV slope maps are shown in Figure 2. The HST image-plane β map is constructed using point-spread function (PSF)-matched WFC3/F105W, F125W, F140W, and F160W images, which trace continua at 2125, 2513, 2805, and 3091 Å in the rest frame respectively. The JWST image-plane β map is constructed from PSF-matched NIRISS/F115W and F150W, corresponding to rest-frame continua at 2315 and 3015 Å. NIRISS/F200W is discarded to avoid potential [O II] $\lambda\lambda 3729, 3726$ and [O III] $\lambda 4363$ emission. The β map constructed from JWST images exhibits more fine structures and variations, thanks to its high spatial resolution. On both image- and source-plane β maps, β spans from -1.5 to -2.5 . The bluest β resides around the compact star clumps, reaching -2.5 , caused by ionizing radiation from massive star formation. On the source plane, we confirm that β varies on the physical scale of < 100 pc.

4. Associated Damped Ly α System with Supersolar Metallicity

The optical spectrum of A2744-arc3, as shown in Figure 3(a), is extracted from the MUSE data cube by making a 2σ deblended segmentation map on a $5'' \times 5''$ white-light image cutout around it. Abundant absorption and emission features are highlighted, including high-column-density Ly α absorption line and the multiplicity of metal absorption lines (e.g., O I $\lambda 1302$, Si II $\lambda 1304$, Si IV $\lambda\lambda 1393, 1402$), strong high-ionization emission lines such as C IV $\lambda\lambda 1548, 1550$, He II $\lambda 1640$, and O III] $\lambda\lambda 1661, 1666$. We also detect a series of intervening Fe II absorbers at $z = 2.582$ along the sightline. The spectral properties of the arc are reported in Table 1.

4.1. Metal-enriched H I Gas with High Column Density

In Figures 3(b) and 3(c), we display the DLA H I and its associated metal absorption-line profiles, respectively. The metal lines exhibit tentative P-Cygni features. We use the Voigt profile to fit absorption lines. The Ly α and Ly β absorption associated with the galaxy at $z = 3.98$, depicted in Figure 3(b), indicates a H I column density of $N_{\text{HI}} = 10^{21.8 \pm 0.1} \text{ cm}^{-2}$, i.e., an extremely strong damped Ly α systems (ESDLA, $N_{\text{HI}} > 5 \times 10^{21} \text{ cm}^{-2}$; Noterdaeme et al. 2014). The measurement is performed using VoigtFit (Krogager 2018), varying b from 20 to 200 km s^{-1} . We then

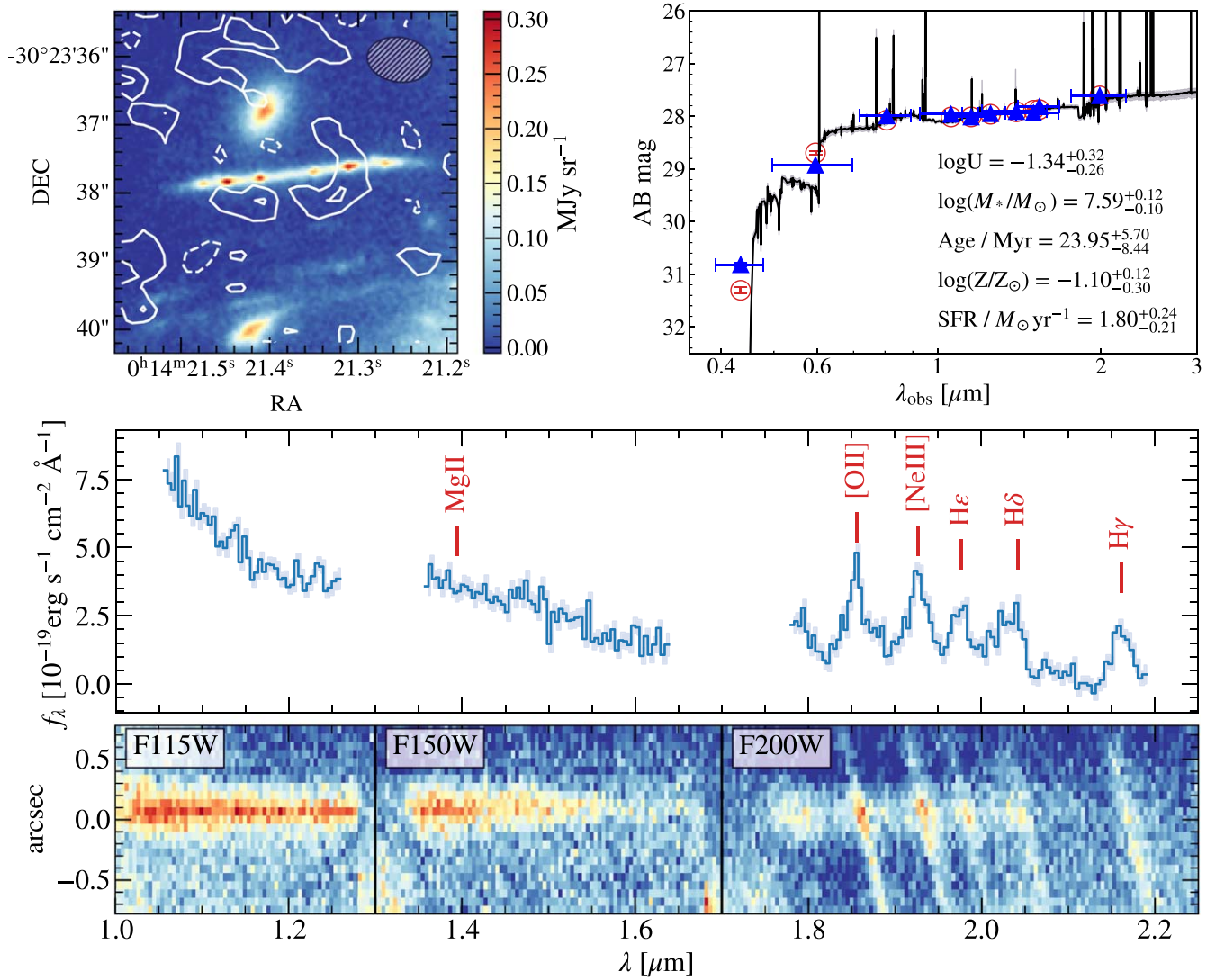


Figure 1. Top left: JWST NIRISS F150W surface brightness image of A2744-arc3 with overlaid continuum contours of ALMA band 6. The contours levels are -2 (white dashed), 1 and 2σ (white solid) with $1\sigma = 44.5 \mu\text{Jy beam}^{-1}$, showing no clear detection at a rest-frame wavelength of 0.23 mm . Top right: photometry and SED fitting for A2744-arc3, with derived physical parameters. Blue triangles denote the measurement and red circles the best-fit result. Bottom: optimally extracted 1D spectra (top panel) and joint 2D spectra covered by NIRISS three filters (F115W, F150W, and F200W). In the top panel, shaded blue regions indicate flux uncertainties, and vertical red lines label common emission lines, among which Mg II is not detected. The 2D spectra of the bottom panel are obtained by summing 2D spectra of the five segments as described in Section 2.1.

add the continuum uncertainty, varying the continuum level by 10%. Tentative detection of residual Ly α emission in the absorption trough might imply partial DLA coverage. Nevertheless, the possibilities of contamination from foreground sources or imperfect sky subtraction cannot be excluded. The source reconstruction in Figure 2 illustrates that the ESDLA extends over at least subkiloparsec scales. Note that VLT/MUSE's seeing leads to a spatial resolution of $\approx 0''.6$, and the six clumps along it have radii of $\lesssim 0''.2$, beyond the spatially resolving capability of MUSE. Thus, we did not show spatially resolved absorption information in this work.

We measure the gas-phase metallicity from the accurate indicator O I. Because O I and H I have similar ionization potentials and are coupled by resonant charge exchange reactions, we then have $[\text{O I}/\text{H I}] \approx [\text{O}/\text{H}]$. Considering the O I $\lambda 1302$ line may be saturated, we estimate the metallicity from both the Voigt profile fitting and curves of growth (CoG) analysis, by varying the Doppler parameter b between 5 and 15 km s^{-1} , the typical values for the intrinsic Doppler parameter

of DLAs as concluded from high-resolution observations (e.g., Penprase et al. 2010; Bashir et al. 2019). We do not adopt large b values (i.e., $b > 20 \text{ km s}^{-1}$) to avoid the underestimation of DLA metallicity without resolving the absorber subcomponent by high-resolution spectroscopy (Prochaska 2006). We list both the Voigt fitting results and the estimates from the curves of growth of metallicity in Table 1 ($b = 10 \text{ km s}^{-1}$). More details about the Voigt fitting results are presented in Appendix C. The estimates from O I and other metal lines such as Si II all yield a supersolar metallicity, with $[\text{O}/\text{H}]$ ranging from ≈ 0.11 to 0.61 and $[\text{Si}/\text{H}]$ from 0.21 to 1.1 (Si II + Si IV) respectively, corresponding to 1.29 – $4.07 Z_{\odot}$ and 1.63 – $12.59 Z_{\odot}$. ($[\text{O}/\text{H}] \approx 0.41$, $[\text{Si}/\text{H}] \approx 0.74$, corresponding to $Z \approx 2.57$ and $5.50 Z_{\odot}$ if assuming $b = 10 \text{ km s}^{-1}$) This metallicity, as highlighted in Figure 3(d), is much higher than the prediction of the cosmic metallicity evolution of DLAs ($[\text{X}/\text{H}] \approx -1.5$ at $z = 3.98$, Rafelski et al. 2012), and the metal abundances of typical star-forming galaxies at $z = 3$ – 5 , measured using nebular emission lines originated from their H II regions (e.g., $[\text{X}/\text{H}] \approx -0.5$ in

Table 1
Physical Properties of the Arc Derived from the Photometry, Absorption, and Emission Features

Basic Physical Parameters										
R.A. (deg)	Decl. (deg)	z_{spec}^a	$\log M_*/M_\odot^b$	Age (Myr)	SFR ($M_\odot \text{ yr}^{-1}$)	$\log U$	μ_{med}^c	μ_1^c	μ_2^c	μ_3^c
3.589089	-30.393844	3.980	$7.59^{+0.12}_{-0.10}$	$23.95^{+5.70}_{-8.44}$	$1.80^{+0.24}_{-0.21}$	$-1.34^{+0.32}_{-0.26}$	45	142	46	30
Absorption Features										
Ion	λ (Å)	CoG Method			Voigt Profile Fitting			$\log(N \text{ cm}^{-2})^g$	$[X/H]^h$	
		EW (Å) ^d	$\log(N \text{ cm}^{-2})^e$	$[X/H]^f$						
H I	1215.670			21.8 ± 0.1^j	...		
O I	1302.168	0.77 ± 0.10	$18.9^{+0.2}_{-0.3}$	$0.41^{+0.20}_{-0.30}$			18.7 ± 0.4	0.21 ± 0.40		
Si II ^k	1260.422	1.12 ± 0.11			
	1304.370	0.47 ± 0.10	$17.8^{+0.4}_{-0.9}$	$0.74^{+0.36}_{-0.53}$			$18.0^{+0.4}_{-0.6}$	$0.81^{+0.36}_{-0.71}$		
Si IV	1402.770	0.67 ± 0.11	17.7 ± 0.3	...			$17.5^{+0.2}_{-1.6}$			
C II ^l	1334.532	1.31 ± 0.09			
Fe II ^k	1608.451	0.80 ± 0.08	18.7 ± 0.2	1.40 ± 0.20			$19.1^{+0.2}_{-0.4}$	$1.80^{+0.20}_{-0.40}$		
Al II	1670.787	0.72 ± 0.10	16.4 ± 0.4	0.15 ± 0.40			$16.4^{+0.3}_{-1.3}$	$0.15^{+0.30}_{-1.30}$		
Emission Lines										
Ion	λ (Å)	EW (Å)	FWHM (km s ⁻¹) ⁱ	Flux (10 ⁻¹⁸ erg s ⁻¹ cm ⁻²)						
C IV	1548.187	3.14 ± 0.23	118 ± 9	7.8 ± 0.6^n						
	1550.772		$<461^m$							
He II	1640.420	1.62 ± 0.09	143 ± 8	3.8 ± 0.2						
O III]	1660.809	6.25 ± 0.27	144 ± 9	3.7 ± 0.2						
	1666.150		139 ± 6	7.9 ± 0.6						
[O II] ^o	3727 ^p	80.2 ± 12.9	...	56.0 ± 6.4						
[Ne III]	3868.760	105.6 ± 16.7	...	66.1 ± 7.3						

Notes. In addition, column densities and abundances of neutral gas metallicity tracers are provided.

^a Redshift determined by O I absorption.

^b Physical parameters are derived from BEAGLE SED fitting.

^c Magnification from the GLAFIC model. μ_{med} is the median value along the arc based on the JWST/NIRISS F115W 2σ profile. μ_1 , μ_2 , and μ_3 is the median magnification of the three mirrored clump pairs from inside (closest to the axis of symmetry/critical curve) to outside respectively.

^d Rest-frame equivalent width of the absorbers. The uncertainties are estimated by varying the continuum level by 10%, combined with the flux uncertainties.

^e Column densities are derived assuming $b = 10 \text{ km s}^{-1}$. Uncertainties are estimated by varying the Doppler parameters b from 5 to 15 km s⁻¹, combined with the uncertainties from EW measurements.

^f $[X/H] = \log(X/H) - \log(X/H)_\odot$. Solar (photosphere) abundances from the compilation by Asplund et al. (2009).

^g Column densities are determined by two-component Voigt profile fits to the absorption features simultaneously, assuming $b = 10 \text{ km s}^{-1}$. We also perform Voigt profile fits using $b = 5$ and 15 km s^{-1} , and the uncertainties presented here include systematics induced by different b values.

^h Metallicities are calculated by summing over column densities of the two Voigt profiles.

ⁱ FWHMs are measured in the rest frame relative to $z = 3.980$, using Gaussian fits and eliminating the effect of MUSE line spread function (Bacon et al. 2017).

^j The uncertainty is determined by varying the continuum level by 10% and the Doppler parameter b from 20 to 200 km s⁻¹.

^k The Si II $\lambda 1260$ and Fe II $\lambda 1608$ absorption might be blended with other lines.

^l The C II $\lambda 1334$ absorption is saturated.

^m The C IV $\lambda 1550$ emission line is likely interfered by noise.

ⁿ There might be potential C IV absorption from neutral gas blended with its emission.

^o Measured from the coadd of JWST/NIRISS slitless spectra as described in Section 2.1. We do not provide FWHMs due to blending effect in grism data and the low resolving power of NIRISS ($R \approx 150$). Flux is measured by fitting single Gaussian profiles to each emission line.

^p The doublet of [O II] at 3726.032 and 3728.815 Å cannot be distinguished.

Troncoso et al. 2014). However, we are cautious to conclude the high metallicity given the low-resolution spectra ($R = 2000\text{--}3000$) and the nondetection of weak lines such as Ni II and Zn II. We need high-resolution spectra to confirm our measurements.

Additionally, we also obtain supersolar metallicity from the Fe II absorption lines. Since Fe II can be depleted onto the dust, the high abundance of Fe II indicates not much dust in both the absorbing gas and the galaxy, consistent with the ALMA millimeter continuum nondetection.

4.2. Strong Narrow Nebular Emission—An Indication of Metal-poor H II Region

A2744-arc3 exhibits significant high-ionization nebular emission in both optical and infrared spectra, e.g., C IV $\lambda 1548$, 1550, He II $\lambda 1640$, O III] $\lambda 1661$, 1666, and [Ne III] $\lambda 3638$ (see Figures 1, 3(a) and Table 1), which have been detected in nearby dwarf galaxies and $z \approx 1\text{--}2$ metal-poor or strong LyC emitting galaxies (e.g., Erb et al. 2010; Schaerer et al. 2022b), but not typically detected in LBGs (e.g., Reddy et al. 2008). These strong narrow nebular emission lines,

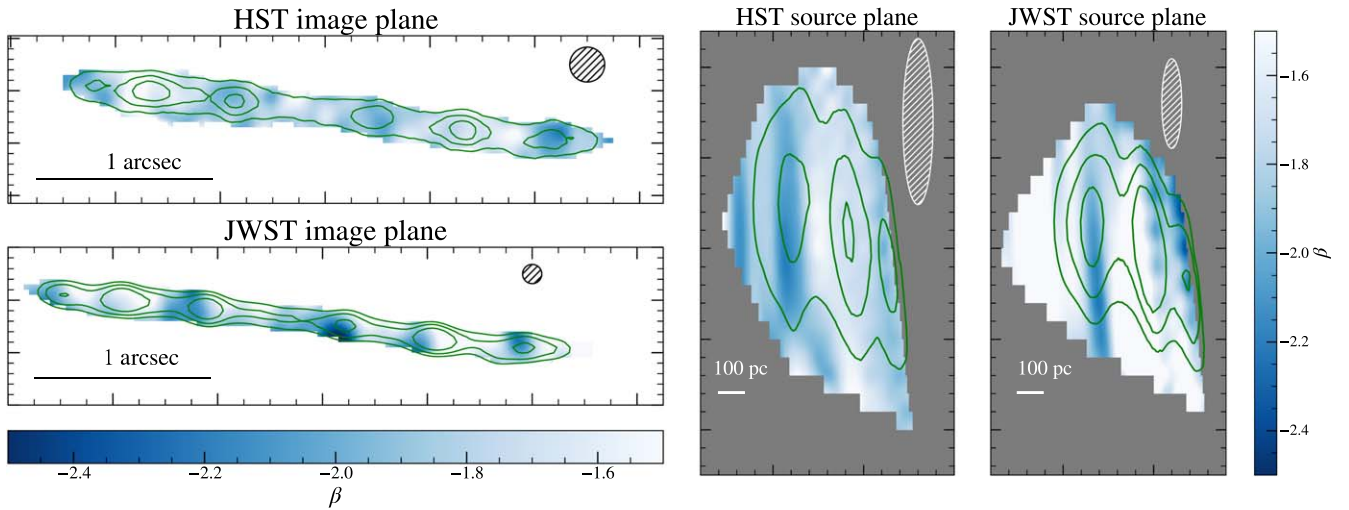


Figure 2. The UV slope β map in the image plane and source plane measured from HST and JWST broadband images. The HST UV slope maps are measured from WFC3/F105W, F125W, F140W, and F160W images (2125–3091 Å in the rest frame), while the JWST UV slope maps are constructed only using NIRISS/F115W and F150W images (2315–3015 Å in the rest frame), to avoid emission lines captured by the NIRISS/F200W filter. The overlaid green contours in HST image/source plane denote the lensed/delensed WFC3/F160W surface brightness levels of 0.05, 0.075, 0.1 MJy sr⁻¹, and the contours in JWST image/source plane show NIRISS/F150W lensed/delensed surface brightness levels of 0.075, 0.1, 0.135 MJy sr⁻¹ respectively. The ellipses on the upper right corners correspond to the FWHM of image/source-plane point-spread function (PSF). Note that source-plane PSF varies among positions due to different magnification and distortion, and the shown one is with the largest FWHM determined by deflection fields at one of the three clumps.

especially He II $\lambda 1640$, are believed to be tightly linked to low-metallicity galaxies with a possible contribution from Population III-like stars (Schaerer 2003; Patrício et al. 2016).

The line ratio between [O II] and [Ne III], two of the principal coolants in H II regions, serves as a metallicity indicator for star-forming galaxies. In A2744-arc3, we obtain $\log([\text{Ne III}]/[\text{O II}]) = 0.07^{+0.06}_{-0.07}$, i.e., $12+\log(\text{O}/\text{H}) = 7.75 \pm 0.05$, based on the empirical metallicity calibrations in Bian et al. (2018), corresponding to $[\text{O}/\text{H}] = -0.94 \pm 0.05$ or $Z/Z_{\odot} = 0.12 \pm 0.01$.²⁰ The mass-metallicity relation in Sanders et al. (2021) predicts $12+\log(\text{O}/\text{H}) = 7.7 \pm 0.1$ for a $M_{*} \approx 10^{7.6 \pm 0.1} M_{\odot}$ galaxy at $z \approx 3.3$; Ma et al. (2016) predicts $12+\log(\text{O}/\text{H}) = 7.27 \pm 0.04$ at $z = 3.98$. These values, including our SED fitting result, are well consistent with models of He II emitters, which favor subsolar metallicities ($\sim 0.1 Z_{\odot}$) and young stellar ages (10^7 – 10^8 yr; Saxena et al. 2020). A further evidence is C IV $\lambda\lambda 1548, 1550$ in pure emission, which is revealed uniquely in galaxies with $12+\log(\text{O}/\text{H}) \lesssim 8$ (Mingozzi et al. 2022). The line ratio of O III] $\lambda 1666$ /He II $\lambda 1640$ is 2.08 ± 0.19 , inconsistent with any photoionization models powered by active galactic nuclei or shocks, which expect more flux in He II $\lambda 1640$ than in O III] $\lambda 1666$ ($\log(\text{O III] } \lambda 1666/\text{He II } \lambda 1640) \approx -3$ to -0.5 (Allen et al. 2008; Feltre et al. 2016; Mainali et al. 2017; Senchyna et al. 2017). This disjoint favors the explanation that the nebular emission in A2744-arc3 should primarily be powered by photoionization due to massive stars (Gutkin et al. 2016).

5. Discussion

5.1. A2744-arc3 Has Properties Similar to Those Local Analogs

SL2S J0217 (James et al. 2014) and SBS 0335-052 (Brammer et al. 2012; Berg et al. 2018; Erb et al. 2019) at lower redshifts

share similar features to A2744-arc3. Strong nebular emission lines such as C IV $\lambda\lambda 1548, 1550$, He II $\lambda 1640$ and O III] $\lambda\lambda 1661, 1666$ are notable in their UV spectrum, suggesting a very high ionizing field from the low-metallicity starbursting region and young stellar populations. SBS 0335-052 is a nearby blue compact dwarf galaxy ($z = 0.0009$) that shows a damped Ly α profile of $\log N_{\text{H I}}/\text{cm}^{-2} = 21.70 \pm 0.05$, while SL2S J0217, a low-mass ($M < 10^9 M_{\odot}$), low-metallicity ($Z < 1/20 Z_{\odot}$) galaxy at $z = 1.8$ magnified by a foreground massive galaxy, may be characterized by a superposition of strong Ly α emission and damped absorption. SL2S J0217 also shows a blue UV slope of $\beta = -1.7 \pm 0.2$ over rest-frame 2100–2800 Å, and an ionization parameter of $\log U \approx -1.5$.

In addition, Green Pea galaxies at $z < 1$ with extremely high degree of ionization in H II regions often present a blend of strong emission and underlying absorption (McKinney et al. 2019), with column densities ranging from $\log N_{\text{H I}}/\text{cm}^{-2} = 19$ –21, well above the LyC thick limit (e.g., Steidel et al. 2018). The presence of the DLA in the spectra of A2744-arc3 at $z = 4$ further suggests that low-mass, low-metallicity galaxies, even at high redshift of $z \gtrsim 4$, may commonly possess abundant neutral hydrogen gas, and the ultimate Ly α and ionizing photon escape may strongly depend on geometrical effects.

5.2. The Metal-enriched Neutral Gas Reservoir around Young, Low-mass, and Metal-poor Galaxies

As discussed above, A2744-arc3 is a low-mass ($M_{*} \approx 10^{7.6} M_{\odot}$) galaxy with low-metallicity ($Z \approx 0.1 Z_{\odot}$) H II regions, estimated from the nebular emission lines. In contrast, metal absorbers associated with the DLA shows that the H I gas around the galaxy may have the supersolar metallicity. Supersolar metallicity of the neutral gas around a low- Z , high- U , and low-mass galaxy is also reported in Berg et al. (2018). The metal-enriched gas can be generated by a high efficiency in the gas cooling and enriched by the recycled inflow from the star formation (e.g., Frye et al. 2019). Due to the metal-enrichment process is rapid, the metal-enriched environment may be further

²⁰ Possible systematics are discussed in Appendix B, e.g., line blending and the scatters of the calibration relation. More observations are expected to confirm its metal abundance.

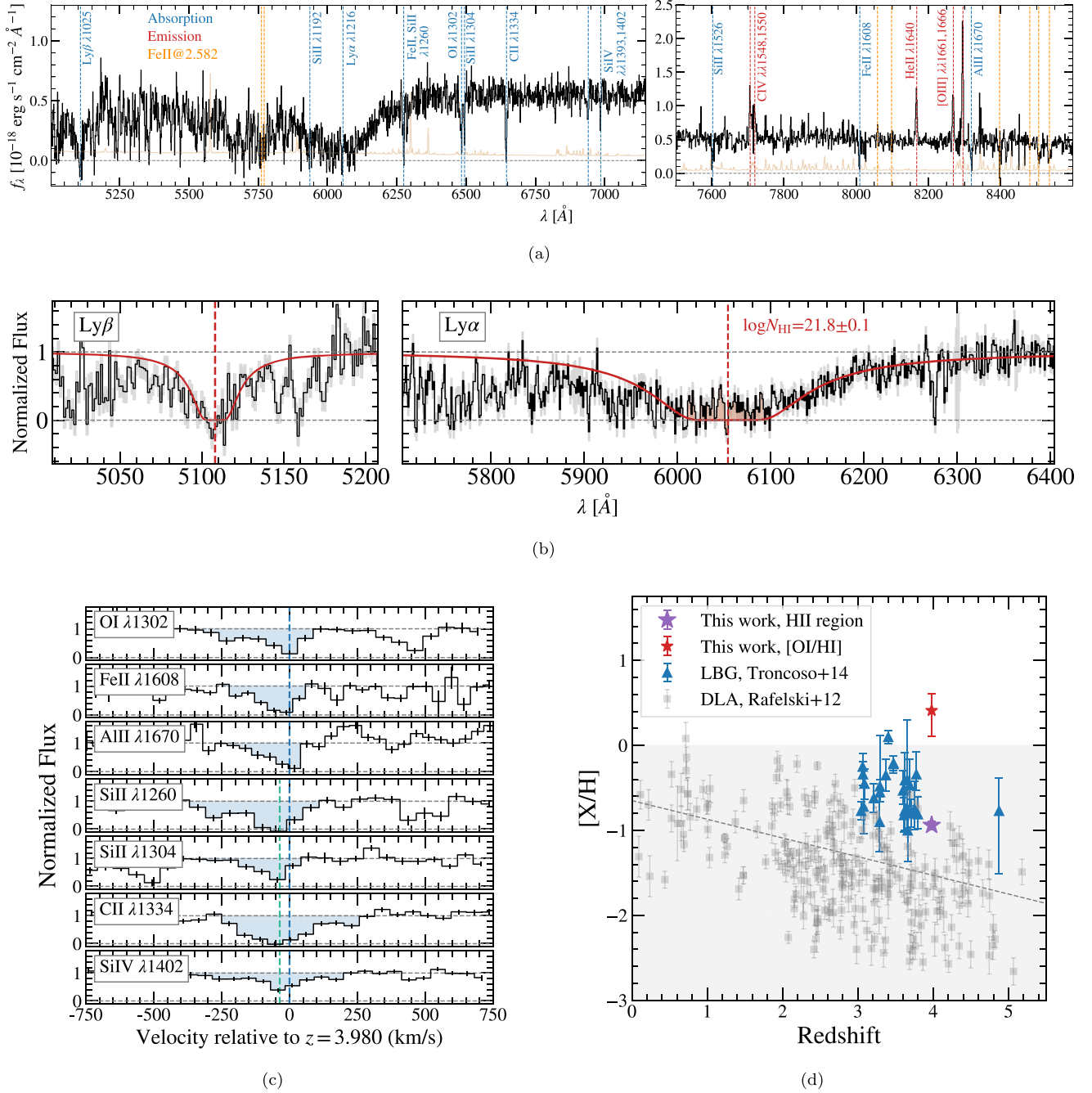


Figure 3. (a) Rest-frame UV spectrum of A2744-arc3 extracted from the VLT/MUSE 3D data cube, with the error spectrum shown in red. Nebular emission lines and absorption features associated with A2744-arc3 are labeled with dashed red and blue lines, respectively. A series of absorption features from an intervening Fe II absorber at $z = 2.582$ are identified in orange. (b) Normalized spectrum zoomed into the DLA Ly α and Ly β line profiles with the Voigt profile fits, with flux uncertainties indicated by gray shaded region. The red solid lines imply the best-fit result yielding $\log(N_{\text{HI}}/\text{cm}^{-2}) = 21.8 \pm 0.1$. Tentative residual in the trough is identified by the red shaded region. (c) Normalized spectrum zoomed into the metal absorption-line profiles. The blue shaded regions are used to measure the equivalent width (EW) of the absorbers. A tentative velocity offset of -36 km s^{-1} relative to $z = 3.980$ (blue dashed) is marked in green dashed lines. (d) The neutral gas metallicity derived from the O I absorber in compared with metal abundances of DLAs (Rafelski et al. 2012; gray squares) and Lyman break galaxies (LBGs; Troncoso et al. 2014; blue triangles) out to $z = 5$. The gray dashed lines indicate the cosmic evolution of DLA metallicities in Rafelski et al. (2012). The gray shaded region marks metallicities lower than solar values. The purple star marks the H II region [O/H] abundance of A2744-arc3 derived from [Ne III]/[O II] empirical metallicity calibrations, as described in Section 4.2.

enhanced by the continuous star formation in the high-redshift universe.

We propose a simple schematic model to explain the metallicity variances in the ISM/CGM and star-forming region at $z \approx 4$, as shown in Figure 4. Massive stars produce a hard radiation field, forming a highly ionized H II region. As mentioned above, the compact star-forming regions could be

surrounded by H I clouds with varying column densities (Erb et al. 2019). DLA can be observed when the sightline is completely blocked by high-column-density neutral clouds, while residual Ly α emission in the absorption trough can be detected in partially obscured cases. These outskirts environments could be metal-polluted by the efficient feedback from massive stars due to the high-velocity stellar wind. The metal-

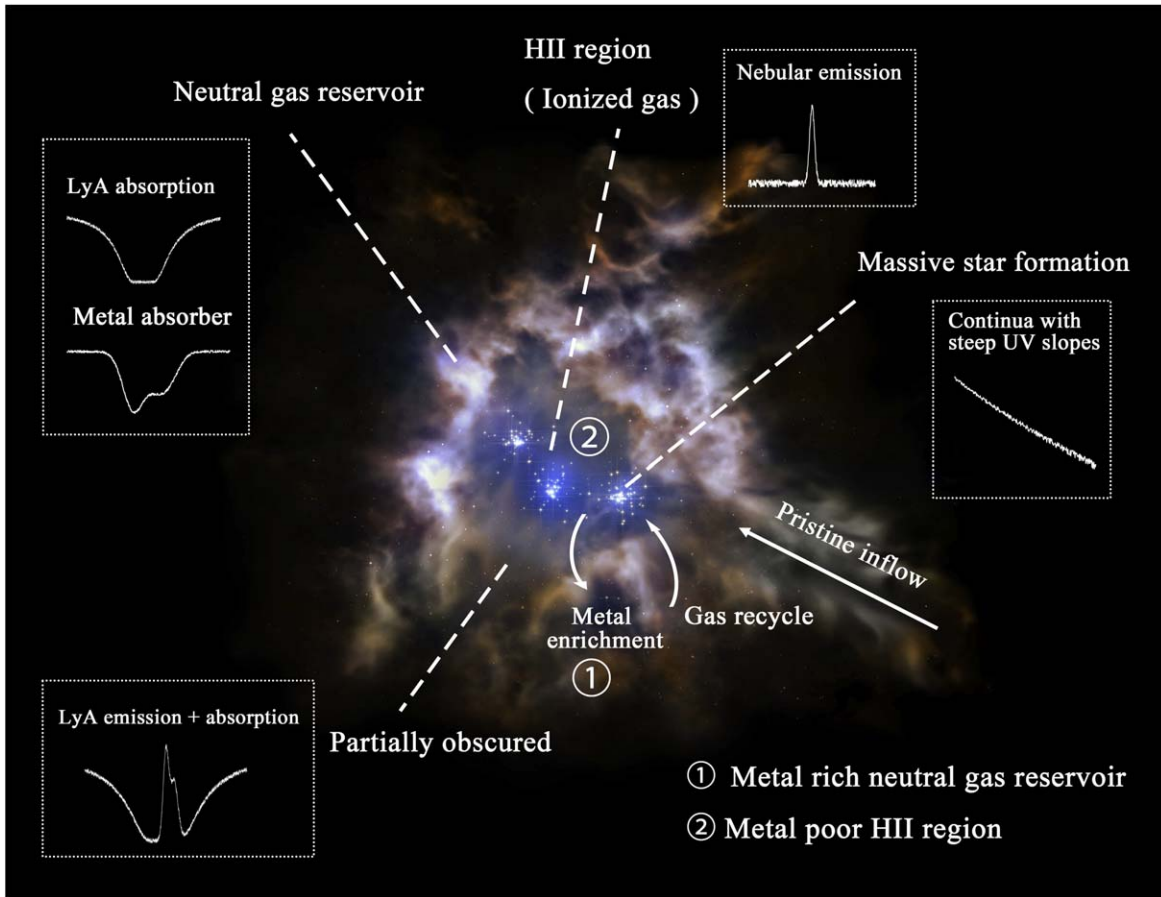


Figure 4. The schematic toy model of A2744-arc3 as a low-mass, low-metallicity galaxy with high-metallicity neutral gas reservoir. The blue stellar clumps inside mark the compact and bursty star-forming regions in A2744-arc3, on scales of subkiloparsecs. Their hard ionization field forms hot, thin, and highly ionized H II regions around them, where strong narrow nebular emission lines are produced. The gas outer layer denotes the neutral gas reservoir with varying column densities in the CGM. Its geometry determines the shape of Ly α emission/absorption we observed. When sightlines are blocked by high-column-density gas, damped Ly α absorption is observed; in partially obscured case, Ly α emission with underlying absorption is observed. Three arrows mark possible gas cycles within the galaxy. Feedback from central star formation, such as stellar winds, could metal enrich the neutral gas, leading to strong metal absorbers with P-Cygni profiles. The recycled neutral gas can further efficiently fuel the next-generation star formation.

enriched gaseous environment could result in the presence of metal absorbers detected in Figure 3(c), sometimes with the detectable P-Cygni profiles (Erb et al. 2012). This scenario explains the tentative detection of Ly α emission shown in Figure 3(b) and asymmetry profiles of metal absorbers shown in Figure 3(c).

Figure 3(d) implies that the metal abundance of A2744-arc3 is tentatively higher than that predicted by cosmic evolution of DLA metallicities. This could be resulted from strong feedback and metal enrichment. To determine whether the enhanced metal enrichment is prevalent among low-mass galaxies, more observations on DLA host galaxies are required.

5.3. Implications of the Spatially Resolved UV Slope Map

The UV continuum slope β ($f_\lambda \propto \lambda^\beta$) is a prominent metric for properties of high-redshift galaxies. Both simulations and observations suggest that bluer galaxies observed at $z = 3-4$ have $\beta = -2$, while values as blue as $\beta = -3$ can in principle be produced by a young (age $\lesssim 10^8$ yr), low-metallicity ($Z \lesssim 10^{-3} Z_\odot$) stellar population (e.g., Schaerer 2003; Jiang et al. 2020; Topping et al. 2022). Bouwens et al. (2010) predicted that the bluest β for low-metallicity ($0.02-0.2 Z_\odot$) starbursts is about -2.7 , consistent with β around the three clumps in Figure 2. This further indicates the low-metallicity

nature of these early star clusters. Aside from the blue radiation from young stars, recombination continuum radiation from the ionized gas can make the UV spectrum redder. When metallicity is greater than $0.02 Z_\odot$, the UV slope generated by the recombination continuum become greater (redder) than -2.5 . With a high spatial resolution, we are able to separate the relatively red nebular continuum emission from the ionized gas from the massive star continuum (e.g., Bouwens et al. 2009), which may be consistent with what we have observed here in A2744-arc3 with JWST.

5.4. Implication of Such a Low-mass, but Dominating Population of Galaxies during Reionization

The UV luminosity of A2744-arc3 is $M_{UV} = -17.8 \pm 0.1$, corresponding to $0.049 L_{UV}^*$ galaxies in the faint end of the galaxy luminosity function ($M^* = -20.88 \pm 0.08$, Bouwens et al. 2015). Through the spatially resolved emission and absorption lines, A2744-arc3 at $z = 4$ provides us with a textbook example, allowing an unparalleled view of low-mass galaxies at the epoch of reionization (EoR).

Low-mass, metal-poor galaxies with hard ionizing radiation show much promise to dominate the ionizing photon budget during EoR (Wise et al. 2014), with a predicted escape fraction of $\sim 20\%$ (Duffy et al. 2014). Similar to lower-redshift analogs

(e.g., James et al. 2014; Berg et al. 2018; Erb et al. 2019), A2744-arc3 at $z=4$ has shown the prevalence of a neutral gas reservoir. Given these observations, we argue that, when modeling the escape of ionizing radiation into the IGM during EoR, the neutral gas reservoir surrounding galaxies themselves (see Figure 4) should be seriously considered. Our identification of the metal-enriched, neutral-gaseous clouds might support the picture that only a small fraction of ionizing radiation of low-mass galaxies escape through the circumgalactic channels with a low column density of neutral gas. With more observations of such galaxies, the statistics of the spatial variations of ionization, metallicity, and H I covering fraction can be better constrained. In particular, the distribution of the optically thick H I clouds could affect the photon escape by geometrical effects. Then, these H I clouds could regulate the star formation and ionization fields through feedback. On the one hand, the outflow from stellar winds could metal enrich the clouds, and then, the clouds could further power the star formation through the recycled inflow (e.g., Frye et al. 2019). In the future, with telescopes such as the Large Ultraviolet Optical Infrared Surveyor (Roberge & Moustakas 2018), we will be able to better constrain the spatial distribution of optically thick H I absorbers at $z=2-5$, and improve our understanding toward the UV photon escape of low-mass galaxies in the high-redshift universe.

6. Conclusion

In this Letter, we presented a detailed analysis on a strongly magnified arclet, A2744-arc3, in the A2744 field with the combination of JWST/NIRISS (both imaging and grism spectroscopy), HST/WFC3, HST/ACS, VLT/MUSE and ALMA observations. The photometry and SED fitting imply that A2744-arc3 has a young age of 24_{-8}^{+6} Myr, high ionization of $\log U$ of -1.3 ± 0.3 , low mass of $\approx 10^{7.6 \pm 0.1} M_{\odot}$, and the low-metallicity H II regions of $12+\log(\text{O}/\text{H}) \approx 7.75$, corresponding to $0.12 Z_{\odot}$ at $z = 3.98$.

The reconstructed source-plane images based on JWST observations provide the resolved UV slope at the spatial resolution of ≈ 100 pc. Three compact clumps show blue UV slopes, ranging approximately from -1.5 to -2.5 , consistent with Vanzella et al. (2022), implying young massive star clusters with bursty star formation activities.

Through absorption studies, we have identified an associated extremely strong DLA system, with $\log N_{\text{H I}} = 21.8 \pm 0.1$. Multiple metal absorbers indicate that this DLA may be supersolar metallicity, with $[\text{O}/\text{H}]$ varying from 0.11 to 0.61 assuming the Doppler parameter b in the range of $5-15 \text{ km s}^{-1}$, higher than typical DLAs and LBGs at similar redshifts, indicative of strong metal enrichment from low-mass galaxies. Additionally, the tentative P-Cygni profiles of the metal lines strengthen evidences for the young stellar feedback. To confirm our conclusion, we need higher resolution spectra with further larger wavelength coverage to measure the absorbing gas-phase metallicity. A2744-arc3 also shows strong narrow nebular emission lines of C IV $\lambda\lambda 1548, 1550$, He II $\lambda 1640$, and O III] $\lambda\lambda 1661, 1666$, indicative of a metal-poor H II region with a hard ionization field.

Combing the lower-redshift analogs SL2S J0217 at $z = 1.8$ and SBS 0335-052 at $z = 0.0009$, our observations of A2744-arc3 at $z=4$ suggest that the neutral gas reservoir may be prevalent around low-mass galaxies. In our schematic model (Figure 4), massive star formation resides within a metal-poor

H II region. The galaxy is surrounded by a large reservoir of neutral gas with a metallicity that could reach solar metallicity. The ionizing photons could only escape through low-column-density channels. A2744-arc3 at $z=4$ provide us an excellent picture in understanding faint-end galaxies that may have played a vital role during the EoR.

X.L. and Z.C. thank Eros Vanzella, Lilan Yang, Dandan Xu, and Shiwu Zhang for very helpful discussions. X.L. thanks Zechang Sun for the useful tool *SpecViewer* (Sun 2021). Z. C., X.L., Y.W., Z.L., M.L., and S.Z. were supported by the National Key R&D Program of China (grant No. 2018YFA0404503), the National Science Foundation of China (grant No. 12073014), and the science research grants from the China Manned Space Project with No. CMS-CSST2021-A05. F. S. acknowledges support from the NRAO Student Observing Support (SOS) award SOSPA7-022. F.S. and E.E. acknowledge funding from JWST/NIRCam contract to the University of Arizona, NAS5-02105. J.X.P. acknowledges partial support from NSF AST-2107991. D.E. acknowledges support from the Beatriz Galindo senior fellowship (BG20/00224) from the Spanish Ministry of Science and Innovation, projects PID2020-114414GB-I00 and PID2020-113689GB-I00 financed by MCIN/AEI/10.13039/501100011033, project P20_00334 financed by the Junta de Andalucía, and project A-FQM-510-UGR20 of the FEDER/Junta de Andalucía-Consejería de Transformación Económica, Industria, Conocimiento y Universidades.

This work is based on observations made with the VLT/MUSE, ALMA, NASA/ESA Hubble Space Telescope and NASA/ESA/CSA James Webb Space Telescope. MUSE observations collected at the European Organisation for Astronomical Research in the Southern Hemisphere under ESO program 094.A-0115. HST and JWST data were obtained from the Mikulski Archive for Space Telescopes at the Space Telescope Science Institute, which is operated by the Association of Universities for Research in Astronomy, Inc., under NASA contract NAS 5-03127 for JWST and NAS 526555 for HST. The JWST observations are associated with program ERS-1324. The HST observations are associated with the Hubble Space Telescope Frontier Fields program. The authors acknowledge the GLASS team for developing their observing program with a zero-exclusive-access period. The following ALMA data is also adopted: ADS/JAO.ALMA#2018.1.00035.L and #2013.1.00999.S. ALMA is a partnership of ESO (representing its member states), NSF (USA), and NINS (Japan), together with NRC (Canada), MOST and ASIAA (Taiwan), and KASI (Republic of Korea), in cooperation with the Republic of Chile. The Joint ALMA Observatory is operated by ESO, AUI/NRAO, and NAOJ. The National Radio Astronomy Observatory is a facility of the National Science Foundation operated under cooperative agreement by Associated Universities, Inc.

Some of the data presented in this paper were obtained from the Mikulski Archive for Space Telescopes (MAST) at the Space Telescope Science Institute. The specific observations analyzed can be accessed via doi:10.17909/T9KK5N and doi:10.17909/91zv-yg35.

Facilities: JWST/NIRISS, ALMA, VLT/MUSE.

Software: JWST calibration pipeline (1.6.2 Bushouse et al. 2022) BEAGLE (Chevallard & Charlot 2016), VoigtFit (Krogager 2018), SpecViewer (Sun et al. 2022).

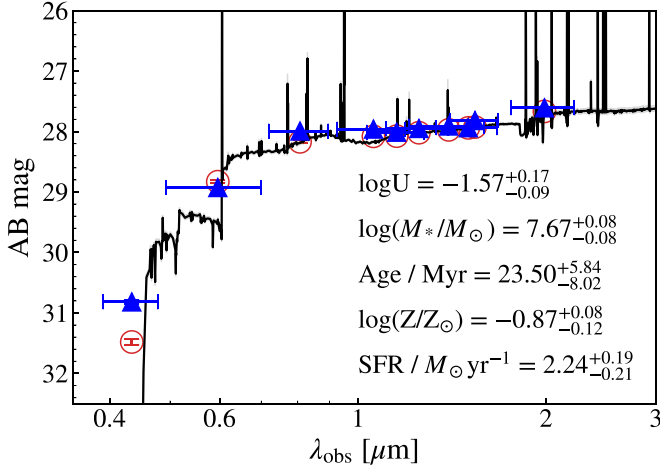


Figure 5. Photometry and SED analysis of A2744-arc3, with delensed fluxes measured using Richard et al. (2021) lensing model. The blue triangles denote the measurement and the red circles the best-fit result. Although the adopted lensing model is different, these R21 results are very consistent with that shown in Figure 1.

Appendix A Systematics of Lensing Models

A.1. Systematics on Photometry

In Section 3.1 we measure the delensed flux of A2744-arc3 using the Glafic lensing model. Here we repeat the measurement using the lensing model in Richard et al. (2021, hereafter R21), and the physical properties of A2744-arc3

keeps consistent with those shown in Figure 5, with the difference of the stellar mass $\approx 1\%$ and age $\approx 2\%$.

A.2. Systematics on Source Reconstruction

In Section 3.2 we adopt the Glafic lensing model to reconstruct the intrinsic UV slope distribution of A2744-arc3. Limited by the lensing model, we can hardly reconstruct the three clump pairs onto the source plane simultaneously, where each pair should have perfectly overlapped. Among all publicly released lensing models, the Glafic model presents the smallest offsets between source-plane positions of these clumps pairs, yielding $0''.010$, $0''.017$, and $0''.033$ from inside to outside respectively. To avoid model-dependent systematics introduced by the nonoverlap, the reconstruction is only performed on the west side of the arclet that is predicted to have larger separation for the three clumps.

Different lensing models yield different magnification and deflection fields, which would lead to different reconstructed morphology. As discussed before, lensing models cannot perfectly recover the symmetric clumps in A2744-arc3 in the source plane, and we choose Glafic because it provides smallest offsets for the reconstructed clump pairs. In Figure 6 we show the reconstructed UV slope using the R21 lensing model, which yields offsets of $0''.12$, $0''.05$ and $0''.19$ for the three clump pairs, as well as the Glafic reconstruction for the arc on the east side. Though the source-plane morphology and layout of the three clumps varies with different lensing models, the UV slope keeps within in the range -2.5 to -1.5 and the spatial variation keeps on scales of <100 pc.

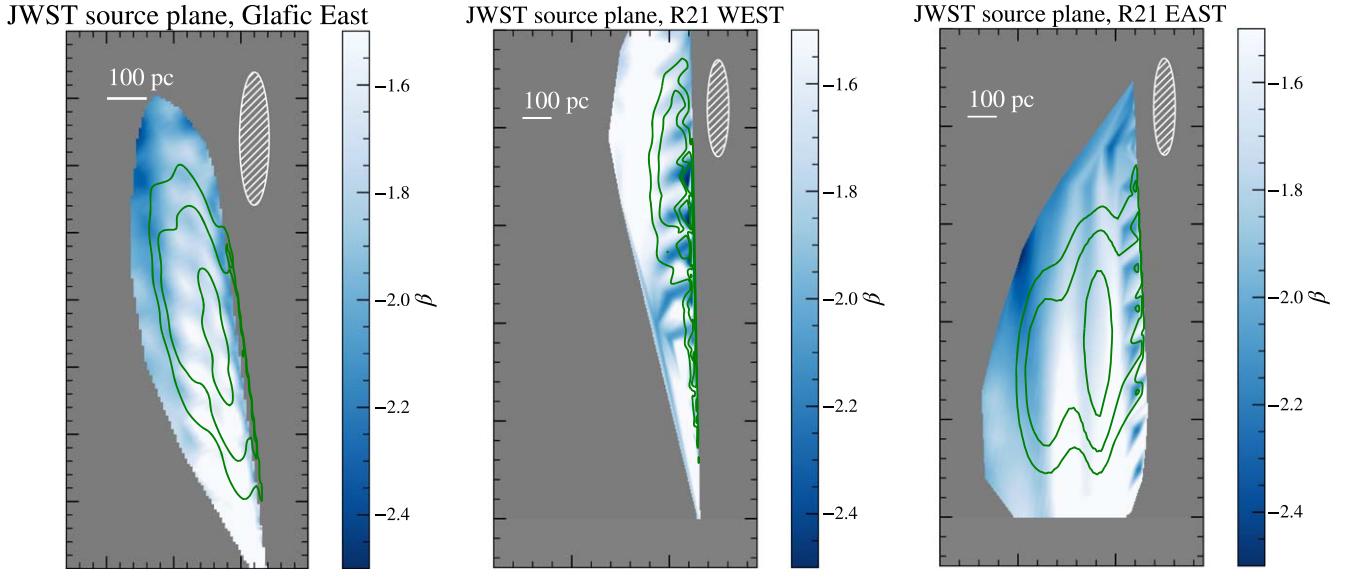


Figure 6. Reconstructed UV slope distribution on the source plane using JWST/NIRISS images. The left panel shows the reconstruction for the east side of A2744-arc3 using the Glafic model. The middle presents the reconstruction for the west side of A2744-arc3 with the R21 model and the right for its east part. See more details in Figure 2.

Appendix B Systematics on Metallicity

In Section 4.2 we estimate the H II region metallicity of A2744-arc3 using the [Ne III]/[O II]-metallicity calibration relation in Bian et al. (2018): $12 + \log(\text{O}/\text{H}) = 7.80 - 0.63 \times \log([\text{Ne III}]/[\text{O II}])$. Due to the low resolving power of JWST/NIRISS ($R \approx 150$), [Ne III] at 3869 \AA is blended with He I+ H8 at 3889 \AA (e.g., Schaerer et al. 2022a), so that the true [Ne III]/[O II] ratio would be lower and hence the metallicity a bit higher than the [Ne III]/[O II]-derived one. But this will not change the metal-poor nature of A2744-arc3. Despite large scatters in the [Ne III]/[O II]-metallicity relation (e.g., Schaerer et al. 2022a) concluded from various galaxies at $z=0-8$, recent observations show that the metallicity of high-redshift galaxies (Sanders et al. 2020; Curti et al. 2022) tends to be consistent with or smaller than the prediction from the empirical calibration in Bian et al. (2018). The latter puts A2744-arc3 to the lower metallicity end. All these facts, along with the

Appendix C Two-component Voigt Profile Fit

In Figure 7 we present the results of simultaneous Voigt profile fits to Al II $\lambda 1670$, Fe II $\lambda 1608$, O I $\lambda 1302$, Si II $\lambda 1526$, and Si IV $\lambda 1402$ absorbers, assuming each absorber has two components. We perform the fits by fixing the Doppler parameter b to 5, 10, 15, as well as 30 km s^{-1} . The column densities and metallicities listed in Table 1 are concluded from estimates with $b = 5, 10$, and 15 km s^{-1} , which is the typical b values for metal absorbers seen in high-resolution spectra (Penprase et al. 2010). However, as discussed in Section 4, a possible large b , e.g., 30 km s^{-1} , due to possible unresolved subcomponents of the absorption profile in low-resolution

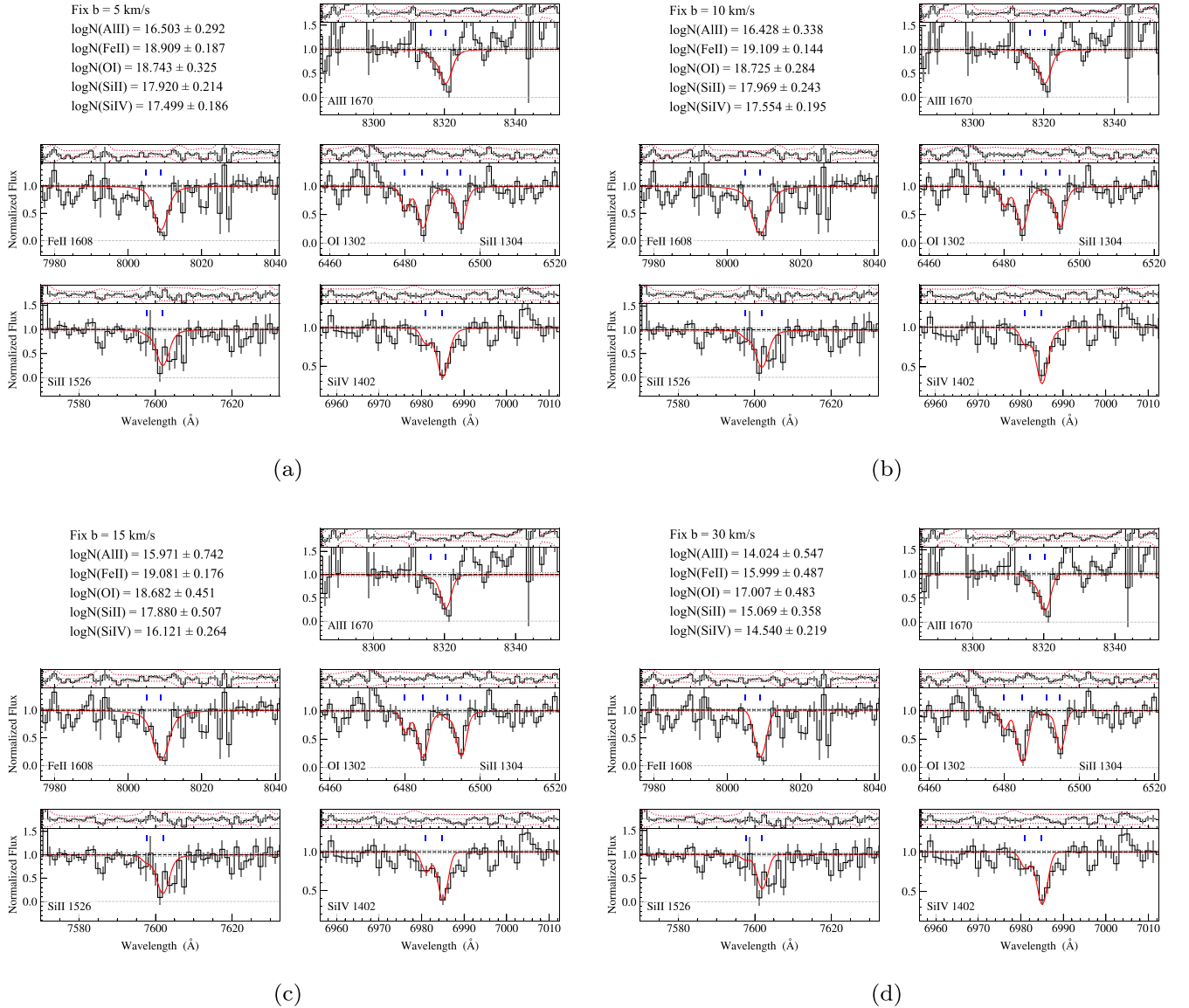


Figure 7. Voigt profile fits to the Al II $\lambda 1670$, Fe II $\lambda 1608$, O I $\lambda 1302$, Si II $\lambda 1526$, and Si IV $\lambda 1402$ absorbers, assuming two components for each absorber and fixing the Doppler parameters b to 5, 10, 15, and 30 km s^{-1} . Red lines are the best-fit profiles and the blue vertical lines mark the positions of the two components for each absorber. The top row of each panel shows residuals of the best-fit profiles (black) and 3σ uncertainties (red dashed). The total column density of each absorber, obtained by summing over their two components, is labeled, in units of $\log N \text{ cm}^{-2}$.

spectra, would yield a lower column density and thus lower metallicity.

ORCID iDs

Xiaojing Lin  <https://orcid.org/0000-0001-6052-4234>
 Zheng Cai  <https://orcid.org/0000-0001-8467-6478>
 Siwei Zou  <https://orcid.org/0000-0002-3983-6484>
 Zihao Li  <https://orcid.org/0000-0001-5951-459X>
 Zuyi Chen  <https://orcid.org/0000-0002-2178-5471>
 Fuyan Bian  <https://orcid.org/0000-0002-1620-0897>
 Fengwu Sun  <https://orcid.org/0000-0002-4622-6617>
 Yiping Shu  <https://orcid.org/0000-0002-9063-698X>
 Yunjing Wu  <https://orcid.org/0000-0003-0111-8249>
 Mingyu Li  <https://orcid.org/0000-0001-6251-649X>
 Jianan Li  <https://orcid.org/0000-0002-1815-4839>
 Xiaohui Fan  <https://orcid.org/0000-0003-3310-0131>
 J. Xavier Prochaska  <https://orcid.org/0000-0002-7738-6875>
 Daniel Schaerer  <https://orcid.org/0000-0001-7144-7182>
 Stephane Charlot  <https://orcid.org/0000-0003-3458-2275>
 Daniel Espada  <https://orcid.org/0000-0002-8726-7685>
 Miroslava Dessauges-Zavadsky  <https://orcid.org/0000-0003-0348-2917>
 Eiichi Egami  <https://orcid.org/0000-0003-1344-9475>
 Kirsten K. Knudsen  <https://orcid.org/0000-0002-7821-8873>
 Gustavo Bruzual  <https://orcid.org/0000-0002-6971-5755>
 Jacopo Chevallard  <https://orcid.org/0000-0002-7636-0534>

References

- Allen, M. G., Groves, B. A., Dopita, M. A., Sutherland, R. S., & Kewley, L. J. 2008, *ApJS*, **178**, 20
- Asplund, M., Grevesse, N., Sauval, A. J., & Scott, P. 2009, *ARA&A*, **47**, 481
- Atek, H., Richard, J., Jauzac, M., et al. 2015, *ApJ*, **814**, 69
- Bacon, R., Conseil, S., Mary, D., et al. 2017, *A&A*, **608**, A1
- Bashir, W., Zafar, T., Khan, F. M., & Chishtie, F. 2019, *NewA*, **66**, 9
- Berg, D. A., Erb, D. K., Auger, M. W., Pettini, M., & Brammer, G. B. 2018, *ApJ*, **859**, 164
- Bergamini, P., Acebron, A., Grillo, C., et al. 2022, arXiv:2207.09416
- Bian, F., Kewley, L. J., & Dopita, M. A. 2018, *ApJ*, **859**, 175
- Bouwens, R. J., Illingworth, G. D., Franx, M., et al. 2009, *ApJ*, **705**, 936
- Bouwens, R. J., Illingworth, G. D., Oesch, P. A., et al. 2010, *ApJL*, **708**, L69
- Bouwens, R. J., Illingworth, G. D., Oesch, P. A., et al. 2015, *ApJ*, **803**, 34
- Bouwens, R. J., Smit, R., Labbé, I., et al. 2016, *ApJ*, **831**, 176
- Brammer, G. B., Sánchez-Janssen, R., Labbé, I., et al. 2012, *ApJL*, **758**, L17
- Bushouse, H., Eisenhamer, J., Dencheva, N., et al. 2022, spacetelescope/jwst: JWST v1.6.2, Zenodo, doi:10.5281/zenodo.6984366
- Chabrier, G. 2003, *PASP*, **115**, 763
- Chen, Z., Stark, D. P., Endsley, R., et al. 2022, arXiv:2207.12657
- Chevallard, J., & Charlot, S. 2016, *MNRAS*, **462**, 1415
- Chisholm, J., Gazagnes, S., Schaerer, D., et al. 2018, *A&A*, **616**, A30
- Curti, M., D'Eugenio, F., Camiani, S., et al. 2022, arXiv:2207.12375
- da Cunha, E., Groves, B., Walter, F., et al. 2013, *ApJ*, **766**, 13
- Duffy, A. R., Wyithe, J. S. B., Mutch, S. J., & Poole, G. B. 2014, *MNRAS*, **443**, 3435
- Erb, D. K., Berg, D. A., Auger, M. W., et al. 2019, *ApJ*, **884**, 7
- Erb, D. K., Pettini, M., Shapley, A. E., et al. 2010, *ApJ*, **719**, 1168
- Erb, D. K., Quider, A. M., Henry, A. L., & Martin, C. L. 2012, *ApJ*, **759**, 26
- Feltre, A., Charlot, S., & Gutkin, J. 2016, *MNRAS*, **456**, 3354
- Flewelling, H. A., Magnier, E. A., Chambers, K. C., et al. 2020, *ApJS*, **251**, 7
- Frye, B. L., Bowen, D. V., Tripp, T. M., et al. 2019, *ApJ*, **872**, 129
- Gronke, M., Dijkstra, M., McCourt, M., & Oh, S. P. 2017, *A&A*, **607**, A71
- Gutkin, J., Charlot, S., & Bruzual, G. 2016, *MNRAS*, **462**, 1757
- James, B. L., Aloisi, A., Heckman, T., Sohn, S. T., & Wolfe, M. A. 2014, *ApJ*, **795**, 109
- Jiang, L., Cohen, S. H., Windhorst, R. A., et al. 2020, *ApJ*, **889**, 90
- Kawamata, R., Oguri, M., Ishigaki, M., Shimasaku, K., & Ouchi, M. 2016, *ApJ*, **819**, 114
- Krogager, J.-K. 2018, arXiv:1803.01187
- Ma, X., Hopkins, P. F., Faucher-Giguère, C.-A., et al. 2016, *MNRAS*, **456**, 2140
- Mahler, G., Richard, J., Clément, B., et al. 2018, *MNRAS*, **473**, 663
- Mainali, R., Kollmeier, J. A., Stark, D. P., et al. 2017, *ApJL*, **836**, L14
- McKinney, J. H., Jaskot, A. E., Oey, M. S., et al. 2019, *ApJ*, **874**, 52
- McMullin, J. P., Waters, B., Schiebel, D., Young, W., & Golap, K. 2007, in ASP Conf. Ser. 376, Astronomical Data Analysis Software and Systems XVI, ed. R. A. Shaw, F. Hill, & D. J. Bell (San Francisco, CA: ASP), 127
- Mingozzi, M., James, B. L., Arellano-Córdova, K. Z., et al. 2022, arXiv:2209.09047
- Murphy, E. J., Condon, J. J., Schinnerer, E., et al. 2011, *ApJ*, **737**, 67
- Noterdaeme, P., Petitjean, P., Pâris, I., et al. 2014, *A&A*, **566**, A24
- Oguri, M. 2010, *PASJ*, **62**, 1017
- Patrício, V., Richard, J., Verhamme, A., et al. 2016, *MNRAS*, **456**, 4191
- Penprase, B. E., Prochaska, J. X., Sargent, W. L. W., Toro-Martinez, I., & Beeler, D. J. 2010, *ApJ*, **721**, 1
- Prochaska, J. X. 2006, *ApJ*, **650**, 272
- Rafelski, M., Wolfe, A. M., Prochaska, J. X., Neeleman, M., & Mendez, A. J. 2012, *ApJ*, **755**, 89
- Ramambason, L., Schaerer, D., Stasińska, G., et al. 2020, *A&A*, **644**, A21
- Reddy, N. A., Steidel, C. C., Pettini, M., et al. 2008, *ApJS*, **175**, 48
- Richard, J., Claeysens, A., Lagattuta, D., et al. 2021, *A&A*, **646**, A83
- Rigby, J., Perrin, M., McElwain, M., et al. 2022, arXiv:2207.05632
- Roberge, A., & Moustakas, L. A. 2018, *NatAs*, **2**, 605
- Sanders, R. L., Shapley, A. E., Jones, T., et al. 2021, *ApJ*, **914**, 19
- Sanders, R. L., Shapley, A. E., Reddy, N. A., et al. 2020, *MNRAS*, **491**, 1427
- Saxena, A., Pentericci, L., Mirabelli, M., et al. 2020, *A&A*, **636**, A47
- Schaerer, D. 2003, *A&A*, **397**, 527
- Schaerer, D., Izotov, Y. I., Worseck, G., et al. 2022b, *A&A*, **658**, L11
- Schaerer, D., Marques-Chaves, R., Barrufet, L., et al. 2022a, arXiv:2207.10034
- Schlawin, E., Leisenring, J., Misselt, K., et al. 2020, *AJ*, **160**, 231
- Senchyna, P., Stark, D. P., Vidal-García, A., et al. 2017, *MNRAS*, **472**, 2608
- Smit, R., Swinbank, A. M., Massey, R., et al. 2017, *MNRAS*, **467**, 3306
- Stark, D. P., Ellis, R. S., Charlot, S., et al. 2017, *MNRAS*, **464**, 469
- Stark, D. P., Richard, J., Siana, B., et al. 2014, *MNRAS*, **445**, 3200
- Steidel, C. C., Bogosavljević, M., Shapley, A. E., et al. 2018, *ApJ*, **869**, 123
- Sun, F., Egami, E., Fujimoto, S., et al. 2022, *ApJ*, **932**, 77
- Sun, Z. 2021, SpecViewer, GitHub <https://github.com/ZechangSun/SpecViewer>
- Topping, M. W., Stark, D. P., Endsley, R., et al. 2022, arXiv:2208.01610
- Treu, T., Roberts-Borsani, G., Bradac, M., et al. 2022, *ApJ*, **935**, 110
- Troncoso, P., Maiolino, R., Sommariva, V., et al. 2014, *A&A*, **563**, A58
- Vanzella, E., Castellano, M., Bergamini, P., et al. 2022, arXiv:2208.00520
- Wise, J. H., Demchenko, V. G., Halicek, M. T., et al. 2014, *MNRAS*, **442**, 2560
- Witstok, J., Smit, R., Maiolino, R., et al. 2021, *MNRAS*, **508**, 1686
- Wu, Y., Cai, Z., Sun, F., et al. 2022, arXiv:2208.08473
- Yang, H., Malhotra, S., Gronke, M., et al. 2017, *ApJ*, **844**, 171
- Yang, H., Wang, J., Zheng, Z.-Y., et al. 2014, *ApJ*, **784**, 35